Supporting information

Nanosensitizer-mediated augmentation of sonodynamic therapy efficacy and antitumor immunity

Yongjiang Li[1,#], Wei Chen[1,#], Yong Kang[2], Xueyan Zhen[1], Zhuoming Zhou[1], Chuang Liu[1], Shuying Chen[1], Xiangang Huang[1], Hai-Jun Liu[1], Seyoung Koo[1], Na Kong[1,3,4], Xiaoyuan Ji[2,4], Tian Xie[4,5,6,7,*], Wei Tao[1,*]

[1] Center for Nanomedicine and Department of Anesthesiology, Brigham and Women's Hospital, Harvard Medical School, Boston, MA 02115, USA

[2] Academy of Medical Engineering and Translational Medicine, Medical College, Tianjin University, Tianjin, 300072, China

[3] Liangzhu Laboratory, Zhejiang University Medical Center, Hangzhou, China

[4] School of Pharmacy, Hangzhou Normal University, Hangzhou, Zhejiang, 311121, China

[5] Key Laboratory of Elemene Class Anti-Cancer Chinese Medicines, Hangzhou Normal University, Hangzhou, Zhejiang, 311121, China

[6] Engineering Laboratory of Development and Application of Traditional Chinese Medicines, Hangzhou Normal University, Hangzhou, Zhejiang, 311121, China

[7] Collaborative Innovation Center of Traditional Chinese Medicines of Zhejiang Province, Hangzhou Normal University, Hangzhou, Zhejiang, 311121, China

[#] These authors contributed equally to this work: Yongjiang Li, Wei Chen

[*] To whom correspondence may be addressed.

Email: tianxie@hznu.edu.cn (T.X.); wtao@bwh.harvard.edu (W.T.)

Contents

Supplementary Figure 18. Gating strategies to identify $CD45^+CD3^+CD4^+$ and $CD45^+CD3^+CD8^+$ T lymphocytes in the tumor, spleen and lymph nodes of 4T1 tumor-bearing mice following the SnSNPs@PEG-mediated treatment strategy.

Supplementary Figure 19. Gating strategies to identify $CD45^+CD3^+CD4^+$ and $CD45^+CD3^+CD8^+$ T lymphocytes in the RIL-175-HCC following the SnSNPs@PEG-mediated treatment strategy.

Supplementary Figure 20. Comparison of immune cell levels in 4T1 tumors in different groups after SnSNPs@PEG-mediated treatment strategy.

Supplementary Figure 21. Flow cytometry analysis of (a) $CD45^+$ cells, (b)(c) $CD45^+CD3^+$ lymphocytes, $CD45^+CD3^+CD4^+$ T lymphocytes and $CD45^+CD3^+CD8^+$ T lymphocytes in RIL-175-HCC after different treatments (n = 3).

Supplementary Figure 22. Comparison of the levels of (a) $CD45^+$ immune cells, (b) $CD45^+CD3^+$ T cells, (c) $CD45^+CD3^+CD4^+$ T cells, and (d) $CD45^+CD3^+CD8^+$ T cells in RIL-175-HCC-bearing mice after various treatments (n = 3).

Supplementary Figure 23. Comparison of $CD45^+CD3^+CD8^+$ T cell levels in spleens and lymph nodes of 4T1 tumor-bearing mice in different groups after SnSNPs@PEG-mediated treatment strategy.

Supplementary Table 1. Comparison of the bandgap of SnSNPs with other nano-sonosensitizers.

Supplementary Table 2. Antibody used for the flow cytometry analysis of T cells.

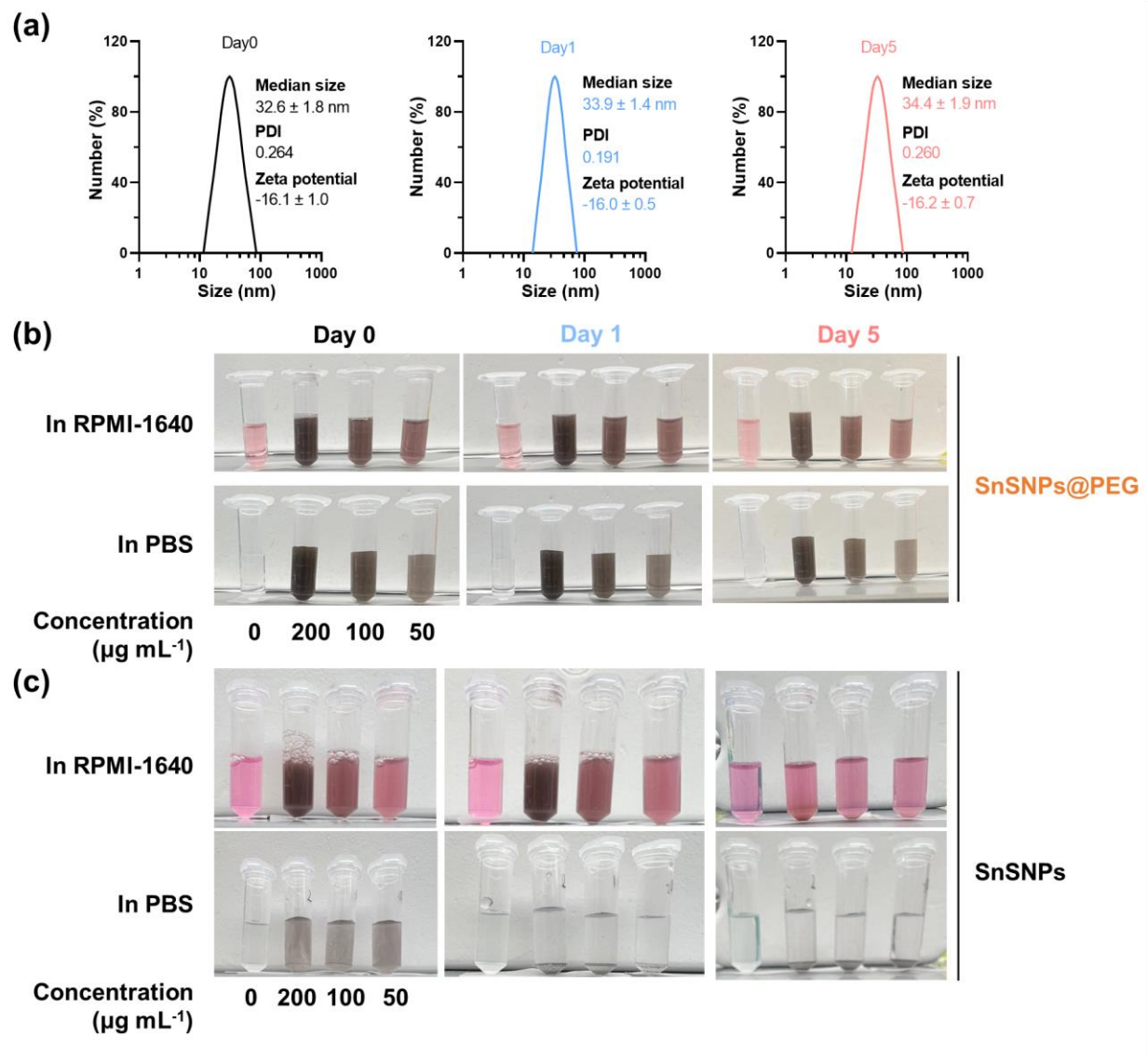

Figure S1. Size distribution, zeta potential and dispersibility of SnSNPs@PEG. a) DLS measurement of size distribution, and zeta potential of SnSNPs@PEG in PBS on different days. b) Photographs showing the dispersion of (b) SnSNPs@PEG and (c) SnSNPs at various concentrations in RPMI-1640 cell culture medium or PBS after incubation at 4 ℃ for different time intervals.

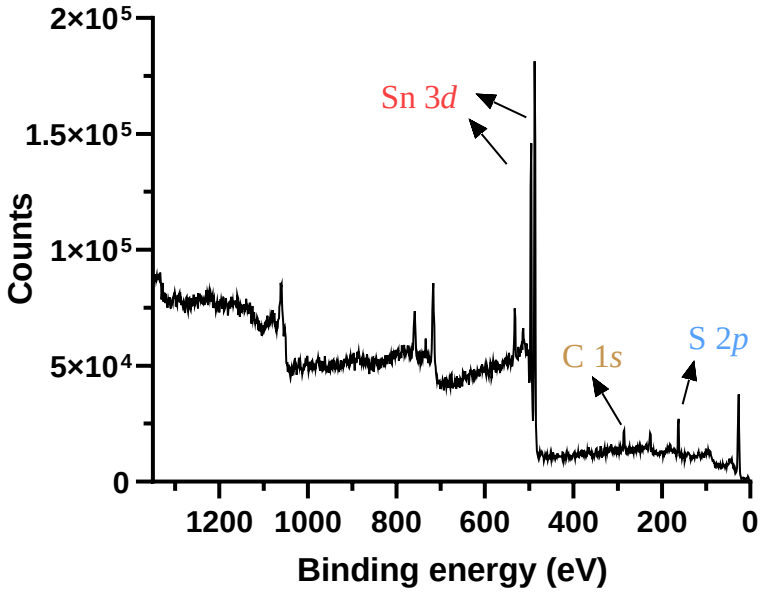

Figure S2. XPS survey spectrum of SnSNPs.

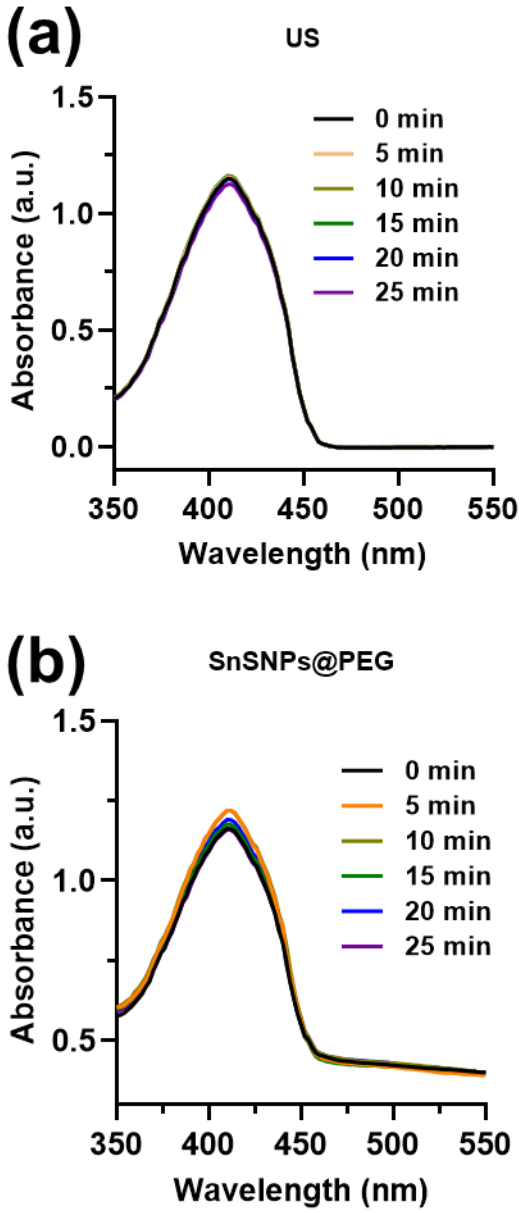

Figure S3. UV−Vis absorbance spectra of the time-dependent oxidation of DPBF (80 μg mL^{-1} in ethanol) by the following treatment: (a) US (1 MHz, 1 W cm^{-2}, 50% duty cycle) only, and (b) SnSNPs@PEG (200 μg mL^{-1}) only.

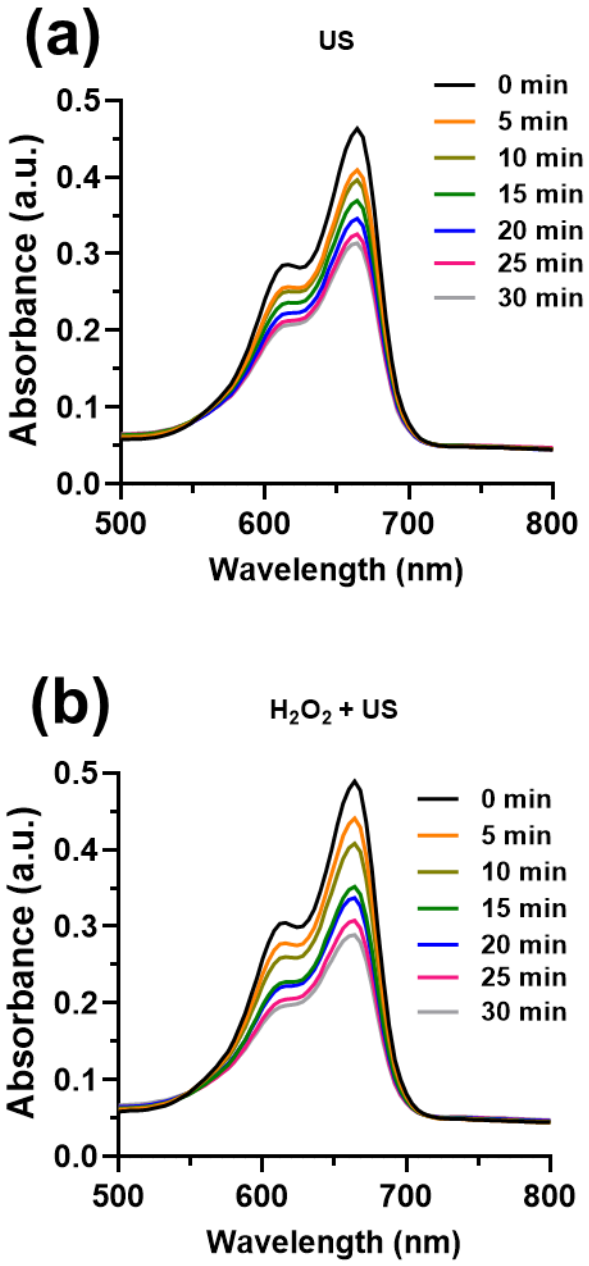

Figure S4. UV−Vis absorbance spectra of the time-dependent oxidation of MB (5 μg mL^{-1} in PBS) by the following treatment: (a) US (1 MHz, 2 W cm^{-2}, 50% duty cycle) only, and (b) H_2O_2 (50 μM) + US.

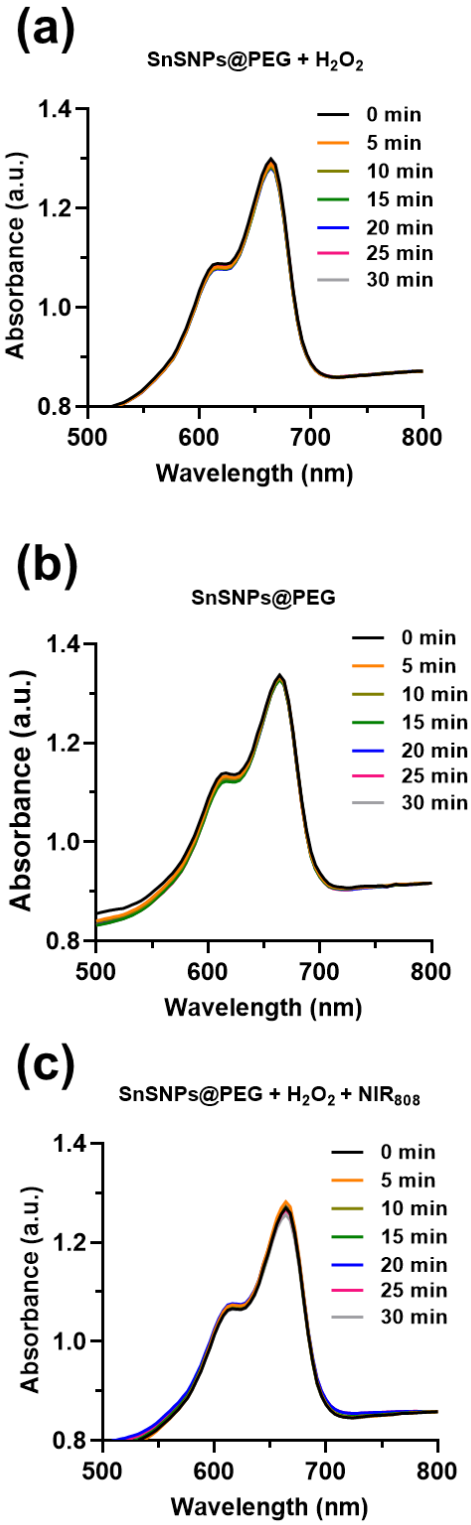

Figure S5. UV−Vis absorbance spectra of the time-dependent oxidation of MB (5 μg mL^{-1} in PBS) by the following treatment: (a) SnSNPs@PEG (100 μg mL^{-1}) + H_2O_2 (50 μM), (b) SnSNPs@PEG only, and (c) SnSNPs@PEG + H_2O_2 + NIR_{808} (1.0 W cm^{-2}).

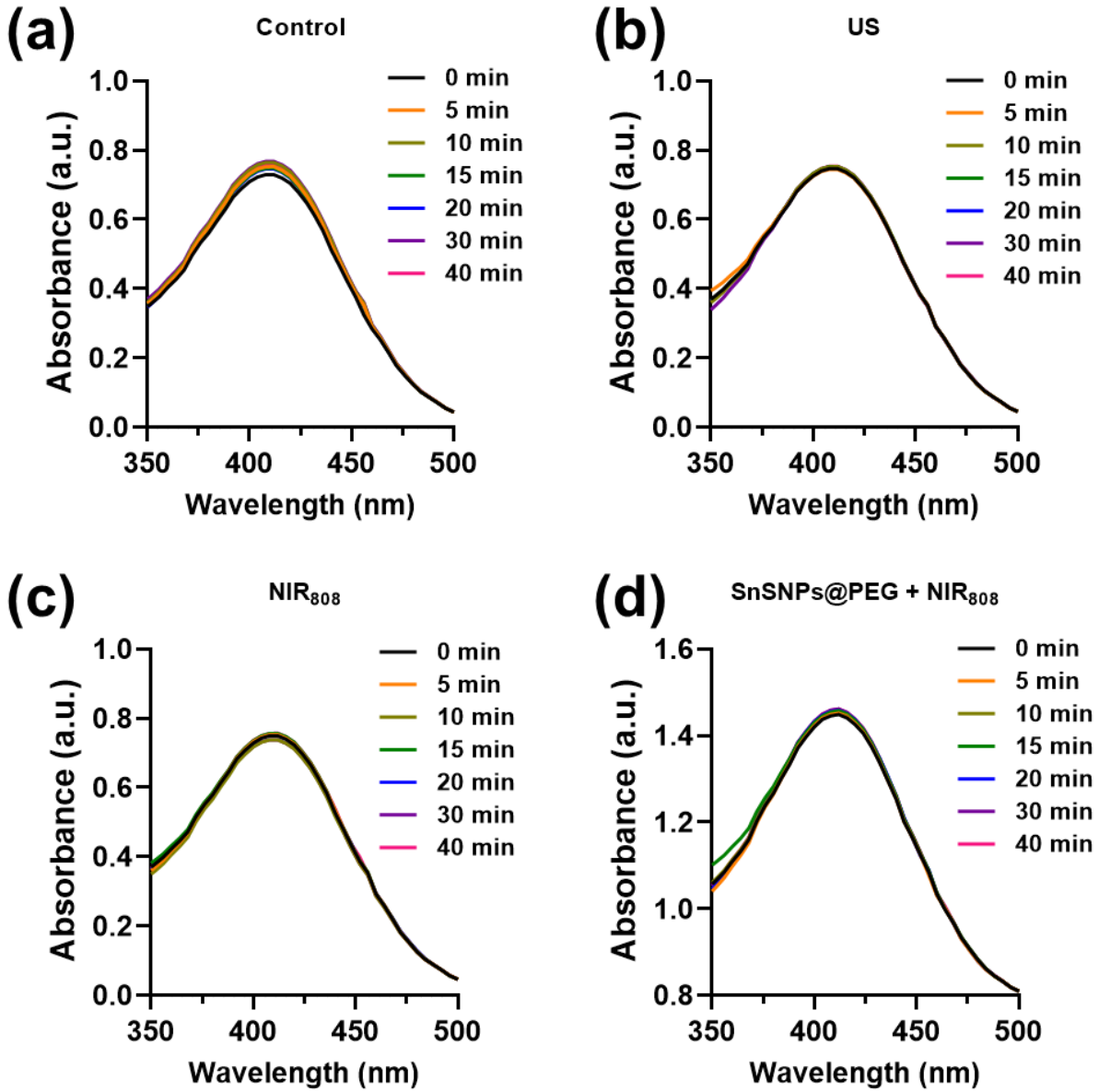

Figure S6. UV−Vis absorbance spectra of the time-dependent oxidation of GSH (30 μg mL^{-1} in PBS) by the following treatment: (a) SnSNPs@PEG (200 μg mL^{-1}), (b) US (1 MHz, 2 W cm^{-2}, 50% duty cycle) only, (c) GSH + NIR_{808} and (d) SnSNPs@PEG + NIR_{808} (1.0 W cm^{-2}).

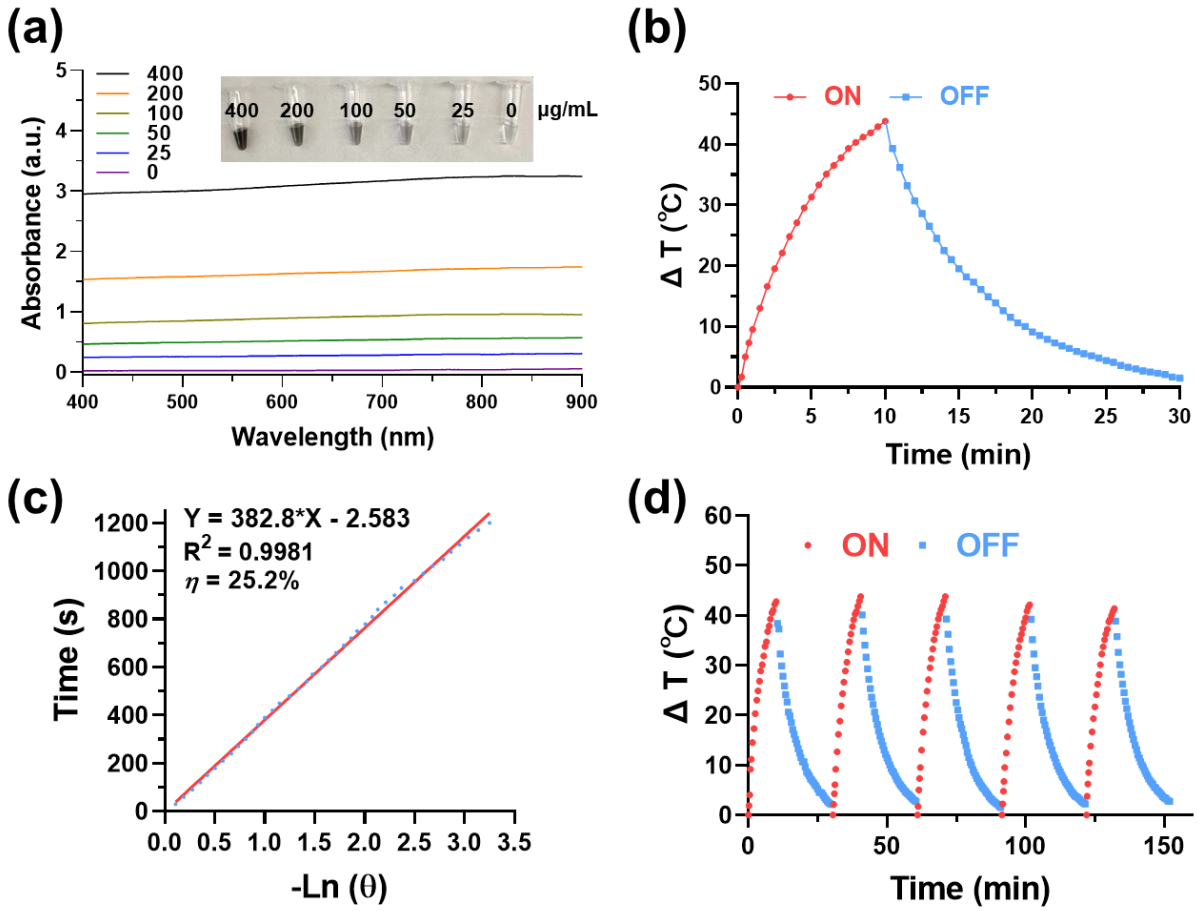

Figure S7. Photothermal performance of SnSNPs@PEG. a) UV-Vis-NIR absorption spectra of SnSNPs@PEG at different concentrations. Inset photo shows SnSNPs@PEG water suspension with the corresponding concentration in µg mL^{-1}. b) Heating and cooling profiles of SnSNPs@PEG (200 µg mL^{-1}) irradiated by an 808 nm NIR laser at the power density of 2.0 W cm^{-2}. c) Liner fitting curve of time and -Ln (θ) from the cooling profile in (b). d) Repetitive five continues heating and cooling profiles of SnSNPs@PEG (200 µg mL^{-1}) irradiated by an 808 nm NIR laser at the power density of 2.0 W cm^{-2}.

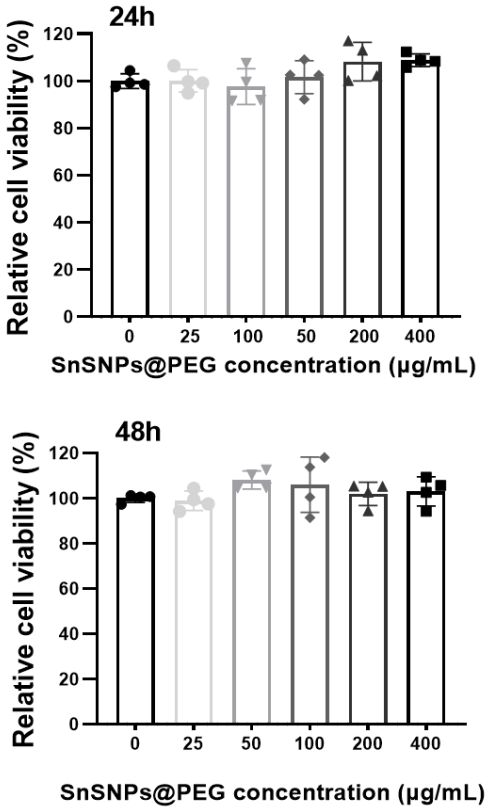

Figure S8. Relative viability of 4T1 cells after incubation with different concentrations of SnSNPs@PEG for 24 and 48 h. Data are from independent samples and are presented as mean ± SD (n = 4).

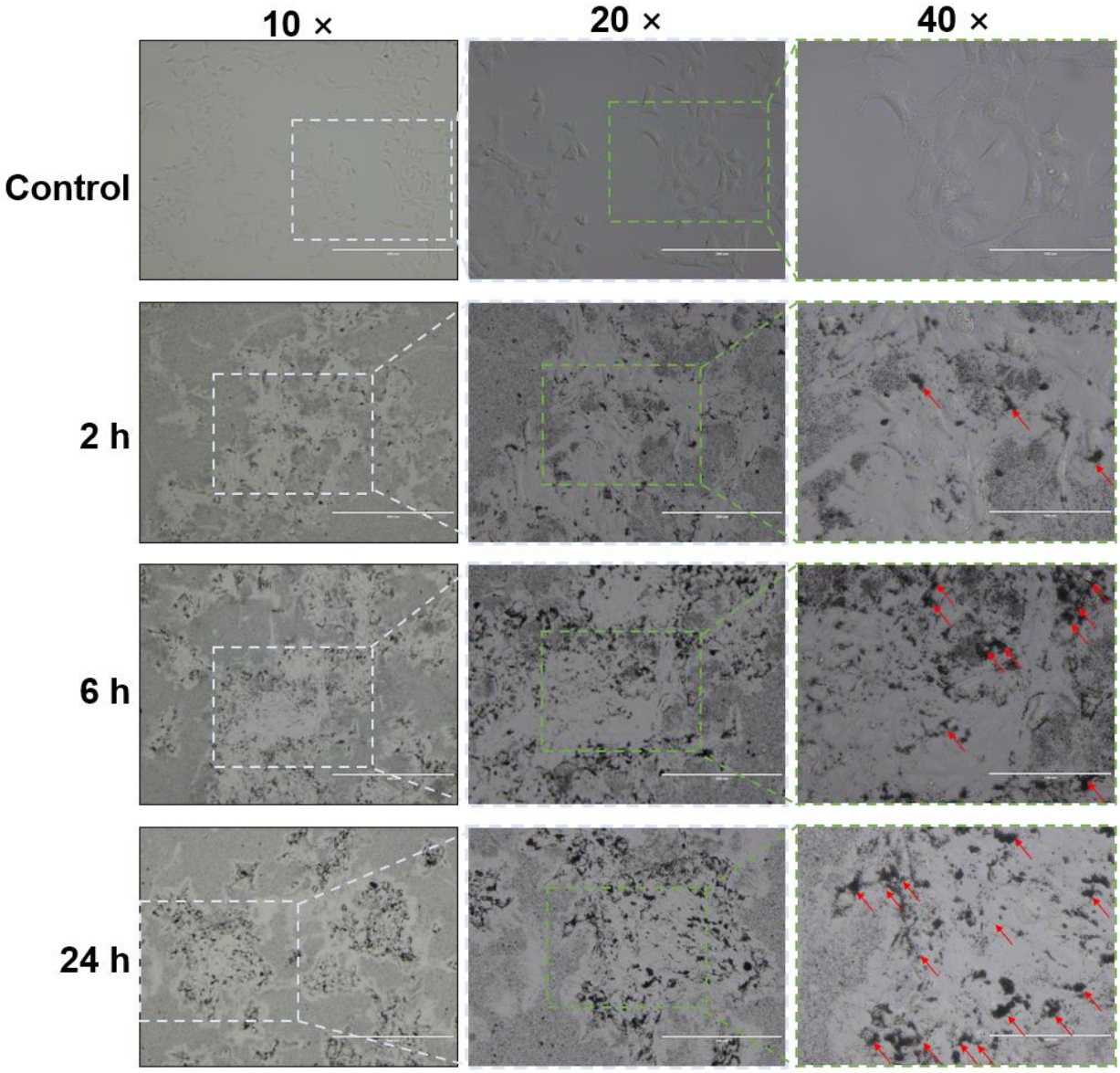

Figure S9. Bright-field microscope images showing time-dependent cellular uptake of SnSNPs@PEG by 4T1 cells. The substantial uptake was highlighted by red arrows. No cytotoxic effect was observed on 4T1 cells given that the substantial cellular uptake of SnSNPs@PEG was observed. Scale bar: 10× = 400 μm, 20× = 200 μm, 40× = 100 μm.

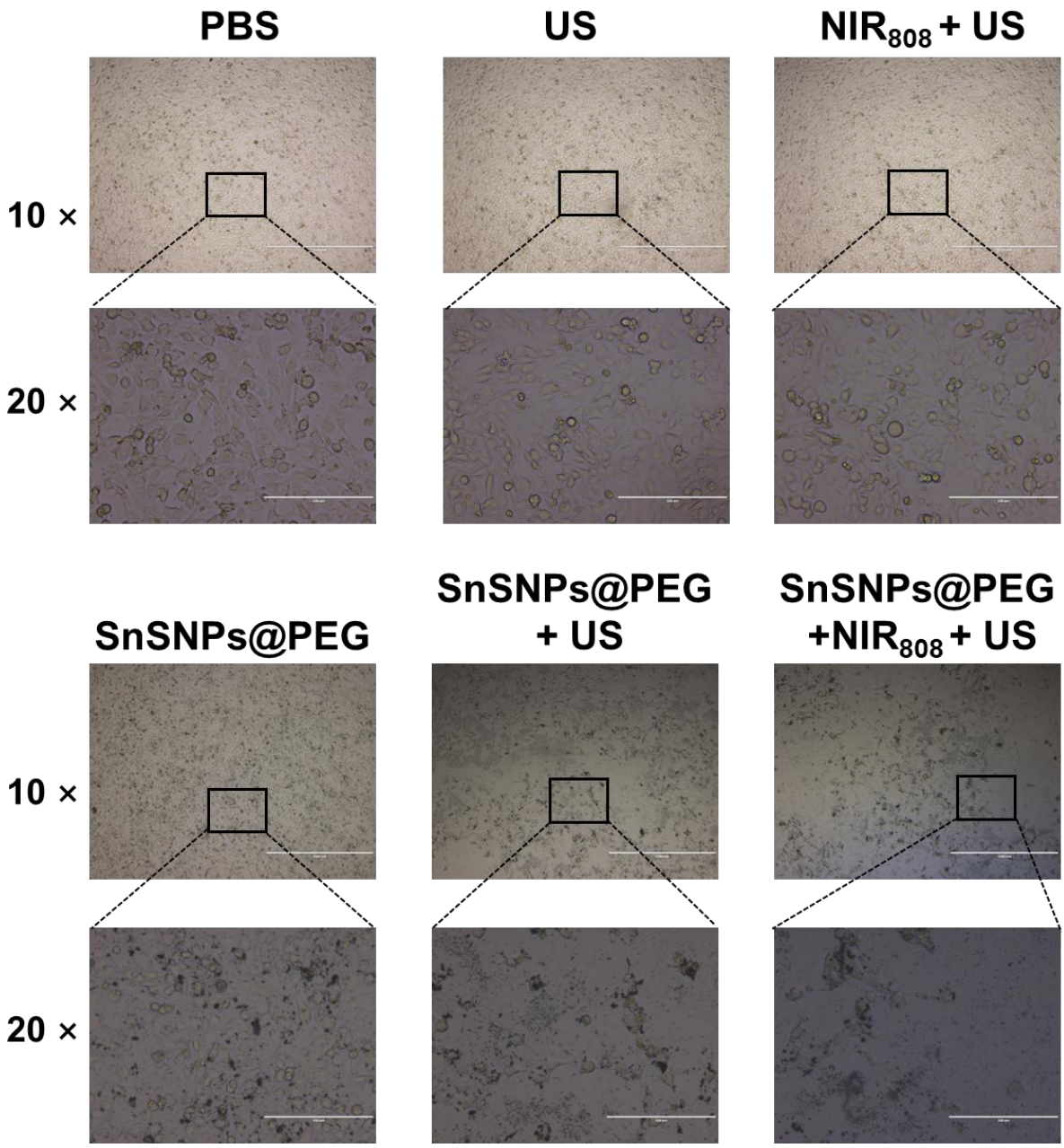

Figure S10. Bright-field microscope images showing 4T1 cells after various treatments. SnSNPs@PEG (200 μg mL^{-1}) with US irradiation (1 MHz, 0.3 W cm^{-2}, 50% duty cycle) or with NIR_{808} (1.0 W cm^{-2}) + US irradiation showed substantial cytotoxic effects. Scale bar: 10 × = 400 μm, 20× = 200 μm.

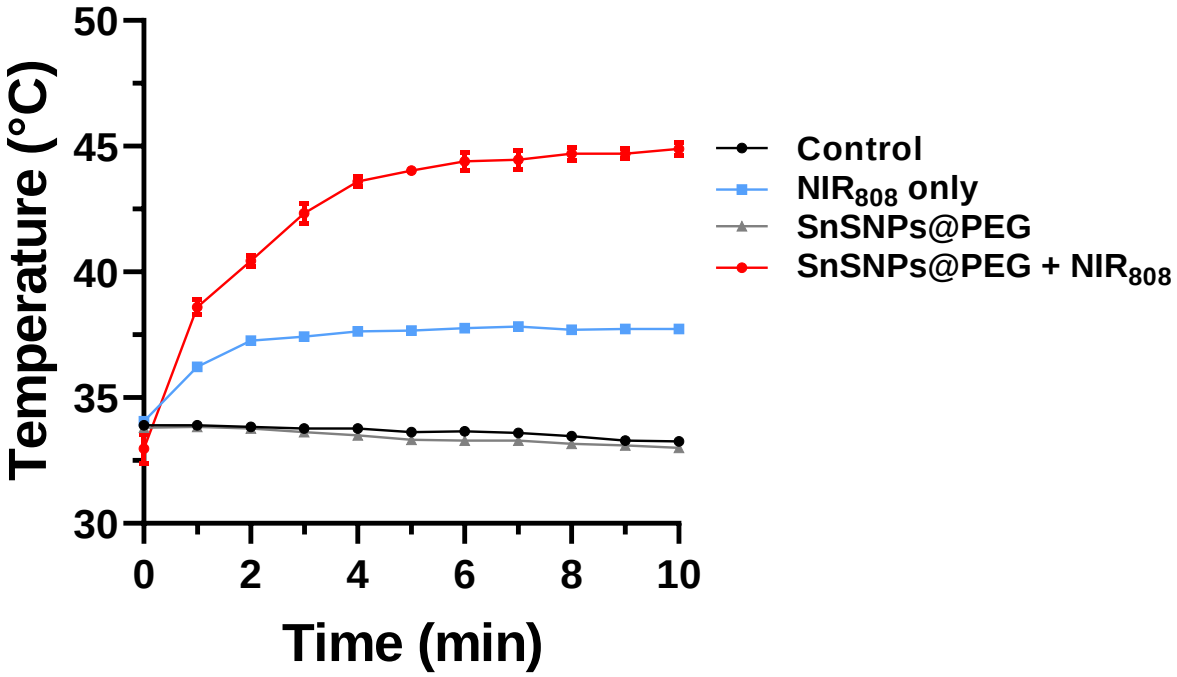

Figure S11. Time-dependent temperature increase profile in 4T1 tumor-bearing mice showing the *in vivo* photothermal effect of SnSNPs@PEG. Temperatures were recorded 12 h after intravenous injection of 100 μL of PBS containing SnSNPs@PEG (10 mg kg^{-1}) under NIR_{808} (1 W cm^{-2}) irradiation. Data are presented as mean ± SD (n = 3).

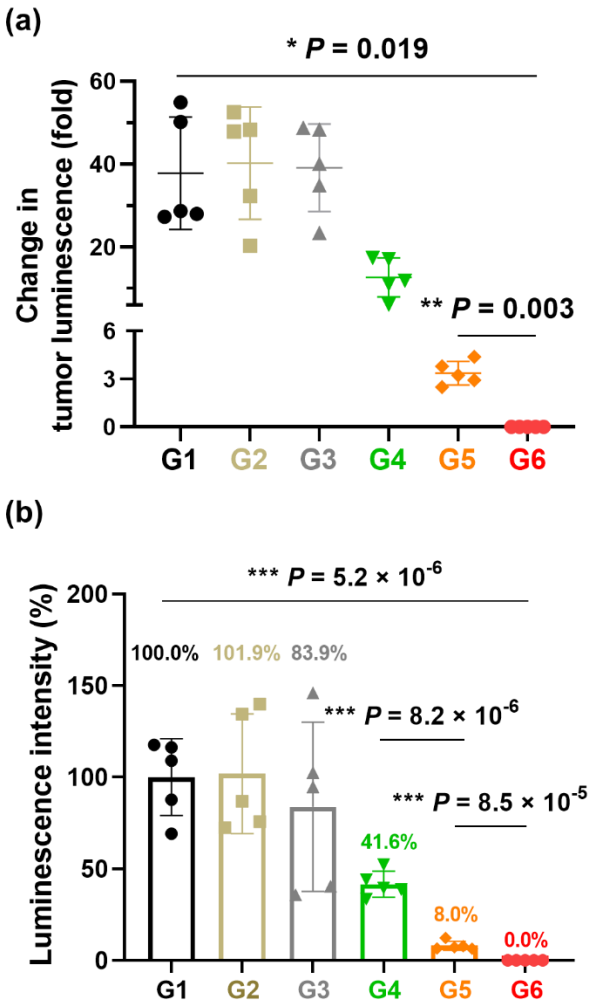

Figure S12. Comparison of luminescence intensity of 4T1 tumor areas after various treatments. (a) Fold-change of tumor luminescence intensity. The intensity change was calculated as luminescence intensity on Day 16/ luminescence intensity on Day 0 (before treatment). (b) Percentage of tumor luminescence intensity. The percentage was calculated as follows: luminescence intensity at Day 16 of each tumor-bearing mice in group/ average luminescence intensity of mice in G1 at Day 16. Statistical analysis between the two groups was performed using two-sided student's *t*-test. ** $P < 0.01$, *** $P < 0.001$. Groups are as follows: control (G1), SnSNPs@PEG (G2), NIR + US (G3), SnSNPs@PEG + US (G4), SnSNPs@PEG + NIR + US (G5), SnSNPs@PEG + NIR + US × 2 (G6), (n = 5).

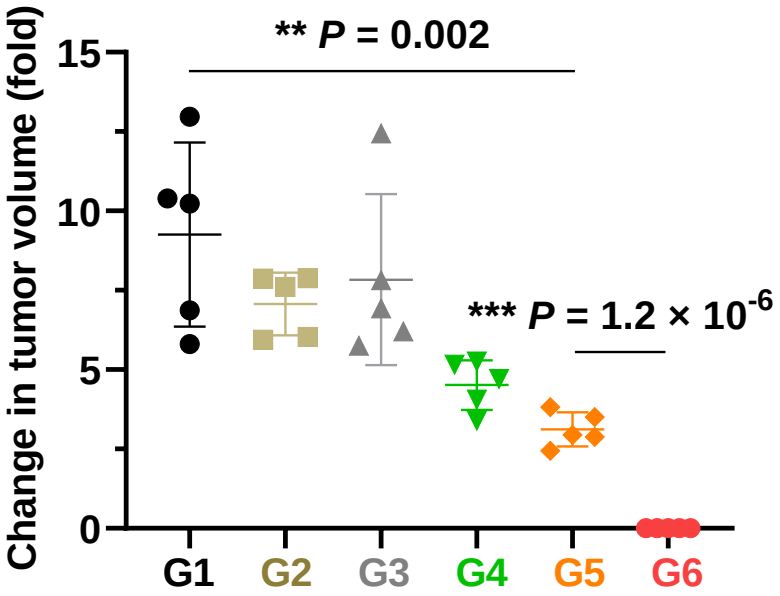

Figure S13. Change in the 4T1 tumor volume after various treatments. The volume change was calculated as follows: tumor volume at Day 16/ tumor volume at Day 0 (before treatment). Data are presented as mean ± SD (n = 5). Statistical analysis between two groups was performed using two-sided student's *t*-test. ** $P < 0.01$, *** $P < 0.001$. Groups are as follows: control (G1), SnSNPs@PEG (G2), NIR + US (G3), SnSNPs@PEG + US (G4), SnSNPs@PEG + NIR + US (G5), SnSNPs@PEG + NIR + US × 2 (G6), (n = 5).

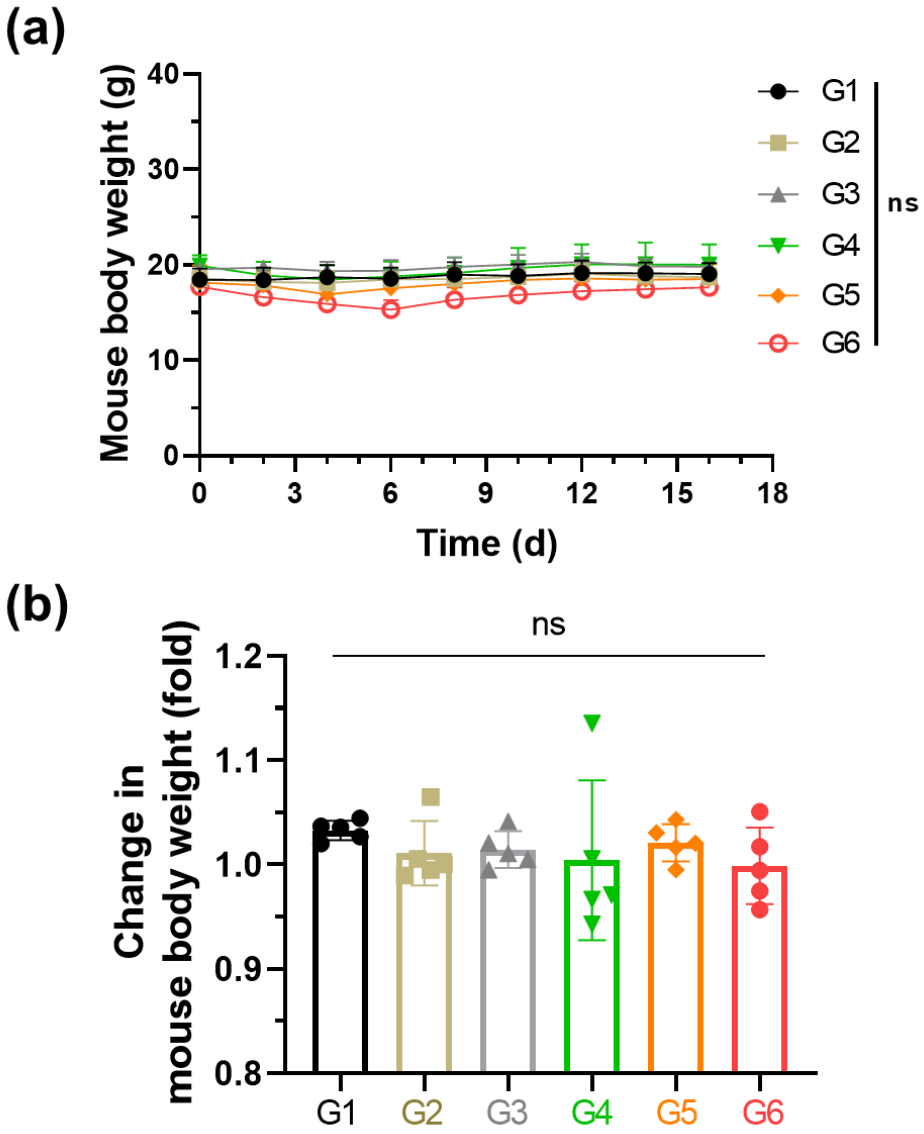

Figure S14. Change in body weight of 4T1 tumor-bearing mice during the SnSNPs@PEG-mediated strategy treatment. (a) Time-dependent body weight of 4T1 tumor-bearing mice of different treatment groups. (n = 5); (b) Change in mouse body weight after various treatments. The mouse body weight change was calculated as follows: mouse body weight at Day 16/ mouse body weight at Day 0 (before treatment). Data are presented as mean ± SD (n = 5). Statistical analysis among groups was performed using one-way ANOVA test. ns, not significant. Groups are as follows: control (G1), SnSNPs@PEG (G2), NIR + US (G3), SnSNPs@PEG + US (G4), SnSNPs@PEG + NIR + US (G5), SnSNPs@PEG + NIR + US × 2 (G6), (n = 5).

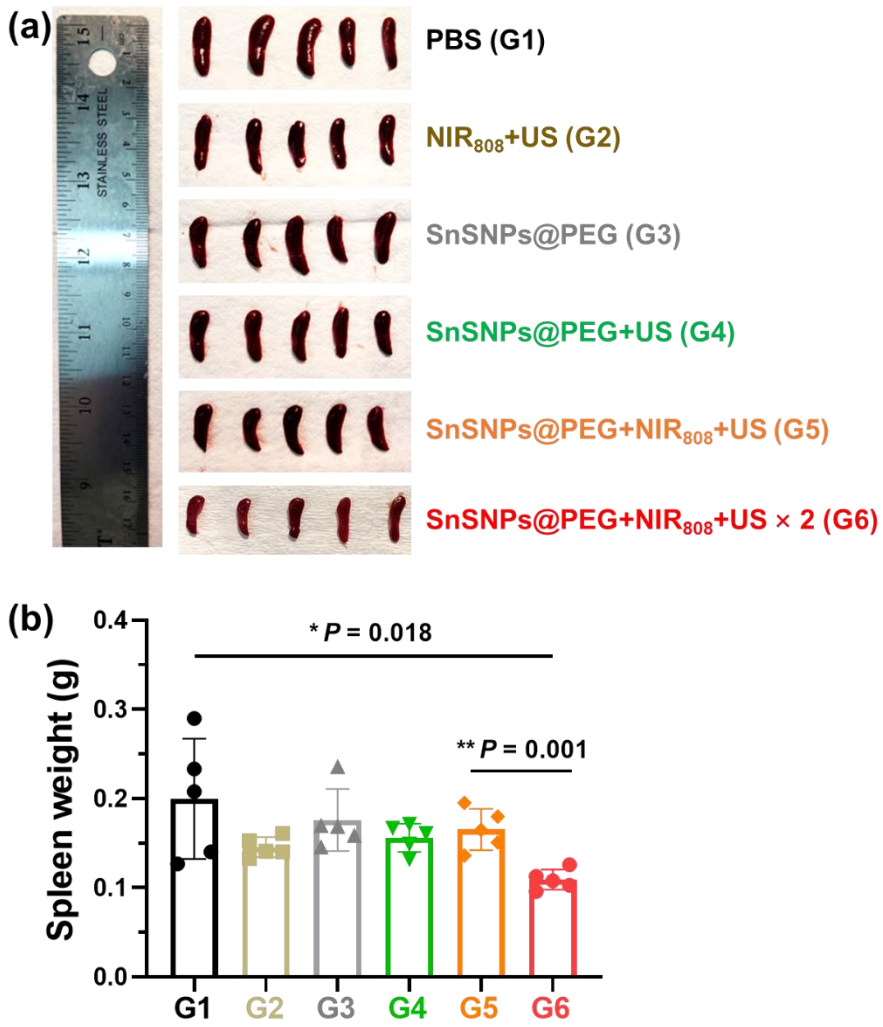

Figure S15. Spleen of 4T1 tumor-bearing mice after SnSNPs@PEG-mediated treatment strategy. (a) Photograph of spleens harvested from 4T1 tumor-bearing mice at Day 16 from different treatment groups (n = 5); b) Spleen weight of 4T1 tumor-bearing mice shown in (a). Data are presented as mean ± SD. (n = 5). Statistical analysis between two groups was performed using student's *t*-test. * $P < 0.05$, ** $P < 0.01$. Groups are as follows: control (G1), SnSNPs@PEG (G2), NIR + US (G3), SnSNPs@PEG + US (G4), SnSNPs@PEG + NIR + US (G5), SnSNPs@PEG + NIR + US × 2 (G6), (n = 5).

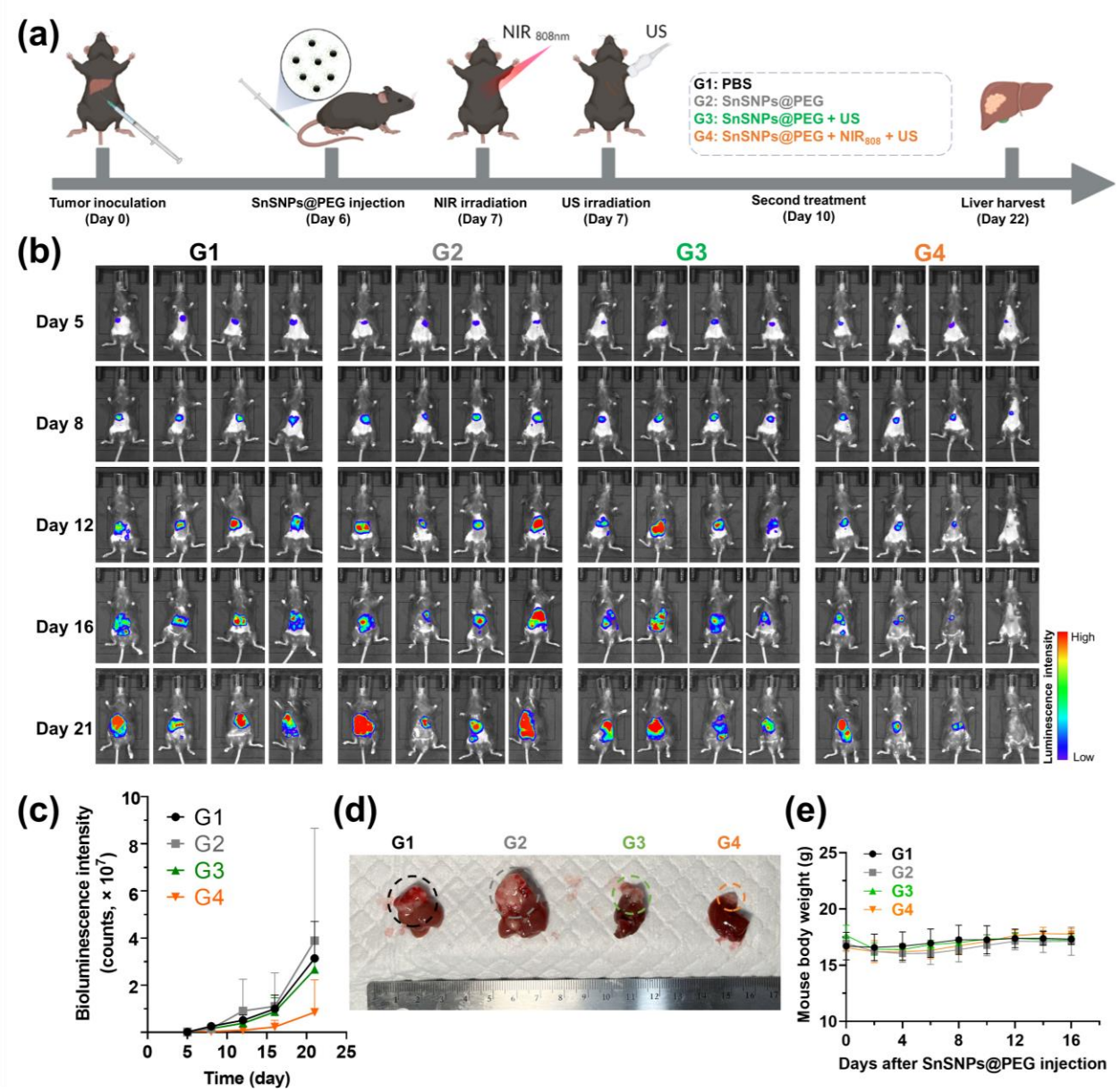

Figure S16. Antitumor efficacy of SnSNPs@PEG-mediated SDT in an orthotopic RIL-175-HCC mouse model. a) Experimental timeline for establishing the RIL-175-HCC mouse model and SnSNPs@PEG-mediated treatment. Illustration was created with BioRender.com. b) Bioluminescence images of orthotopic RIL-175-HCC-bearing mice before, during and after various treatments, including PBS (G1), SnSNPs@PEG (G2), SnSNPs@PEG + US (G3), and SnSNPs@PEG + NIR_{808} + US (G4). The injection volume is 100 μL and the dose of SnSNPs@PEG is 10 mg kg^{-1}. c) Analysis of bioluminescence (counts) of orthotopic RIL-175-HCC-bearing mice before, during and after various treatments. Data are presented as mean ± SD (n = 4). d) Photograph of excised livers with RIL-175-HCC after various treatments (Day 22). Tumor areas are highlighted by circles. e) Time-dependent body weight of RIL-175-HCC-bearing mice after receiving various treatments.

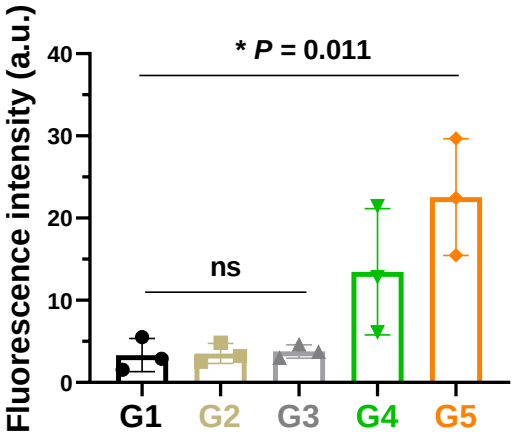

Figure S17. Semi-quantitative analysis of green fluorescence intensity showing the ROS level in tumors of 4T1 tumor-bearing mice after various treatments. Data are presented as mean ± SD (n = 3). Statistical analysis between two groups was performed using student's *t*-test. * $P < 0.05$. Groups are as follows: control (G1), NIR + US (G2), SnSNPs@PEG (G3), SnSNPs@PEG + US (G4), SnSNPs@PEG + NIR + US (G5), (n = 3).

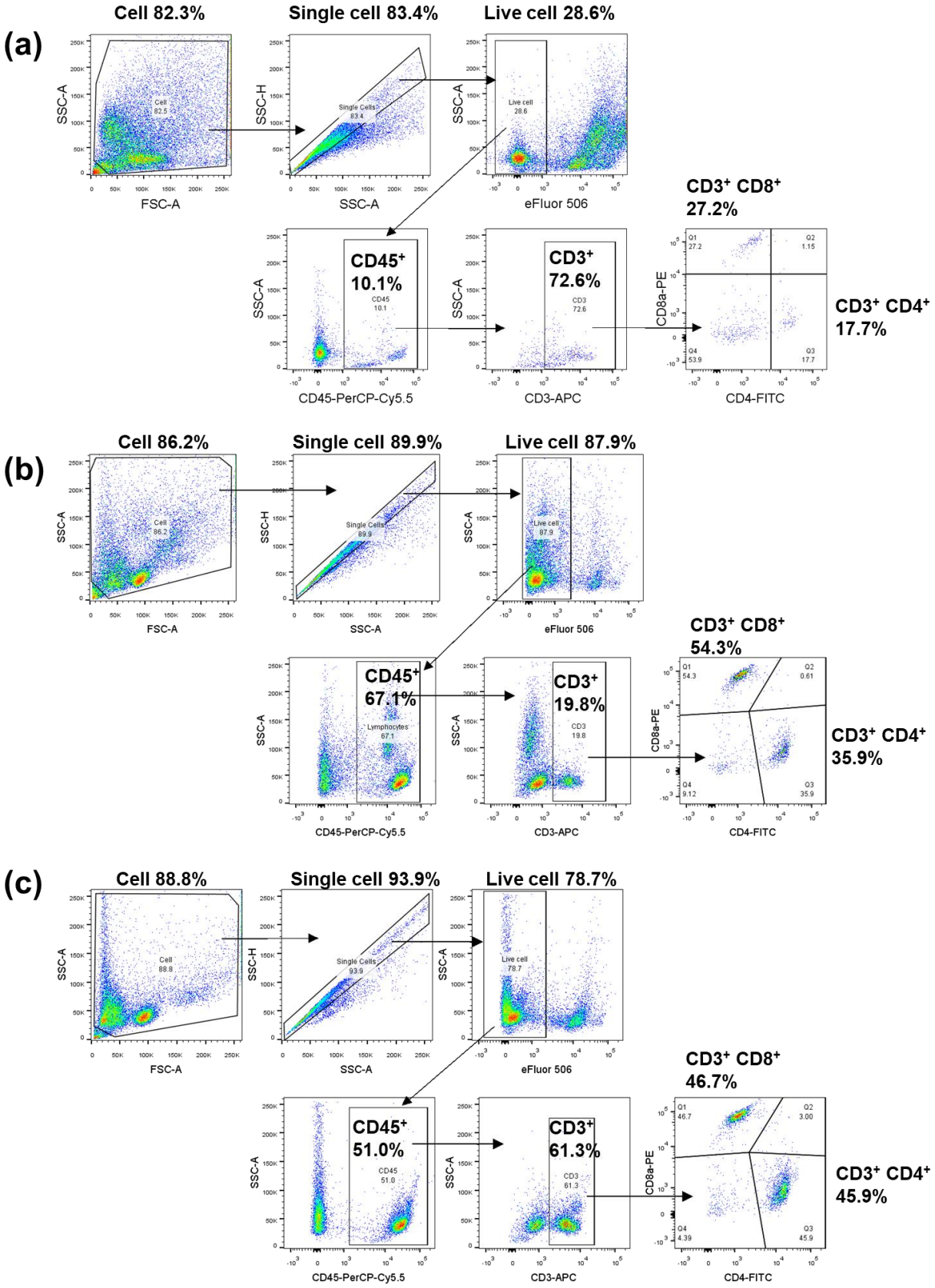
(a)
Cell 82.3%
Single cell 83.4%
Live cell 28.6%
SSC-A
FSC-A
SSC-H
SSC-A
SSC-A
eFluor 506
CD45+ 10.1%
CD45-PerCP-Cy5.5
CD3+ 72.6%
CD3-APC
CD3+ CD8+ 27.2%
CD8a-PE
CD4-FITC
CD3+ CD4+ 17.7%
(b)
Cell 86.2%
Single cell 89.9%
Live cell 87.9%
CD45+ 67.1%
CD3+ 19.8%
CD3+ CD8+ 54.3%
CD3+ CD4+ 35.9%
(c)
Cell 88.8%
Single cell 93.9%
Live cell 78.7%
CD45+ 51.0%
CD3+ 61.3%
CD3+ CD8+ 46.7%
CD3+ CD4+ 45.9%

Figure S18. Gating strategies to identify $CD45^+CD3^+CD4^+$ and $CD45^+CD3^+CD8^+$ T lymphocytes in the tumor, spleen and lymph nodes of 4T1 tumor-bearing mice following the SnSNPs@PEG-mediated treatment strategy. (a) tumor, (b) spleen and (c) lymph node. Single live cells were first gated, followed by a selection of $CD45^+CD3^+$ T lymphocytes. Subsequently, the populations of $CD45^+CD3^+CD4^+$ and $CD45^+CD3^+CD8^+$ T lymphocytes were distinguished and analyzed.

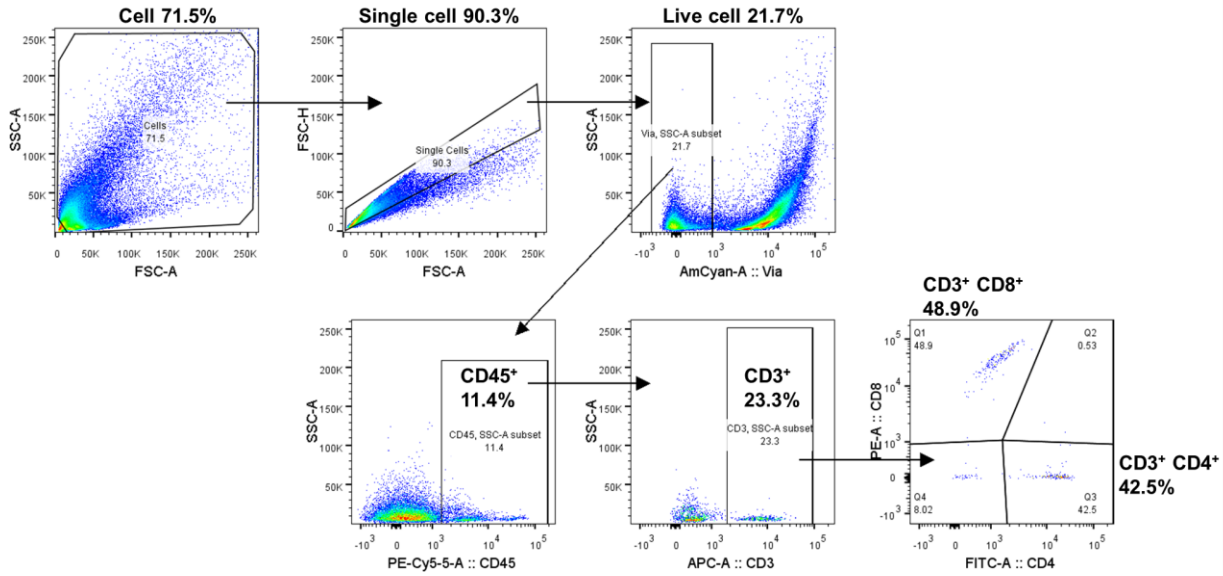

Figure S19. Gating strategy to identify $CD45^+CD3^+CD4^+$ and $CD45^+CD3^+CD8^+$ T lymphocytes in the RIL-175-HCC following the SnSNPs@PEG-mediated treatment strategy. Single live cells were first gated, followed by a selection of $CD45^+CD3^+$ T lymphocytes. Subsequently, the populations of $CD45^+CD3^+CD4^+$ and $CD45^+CD3^+CD8^+$ T lymphocytes were distinguished and analyzed.

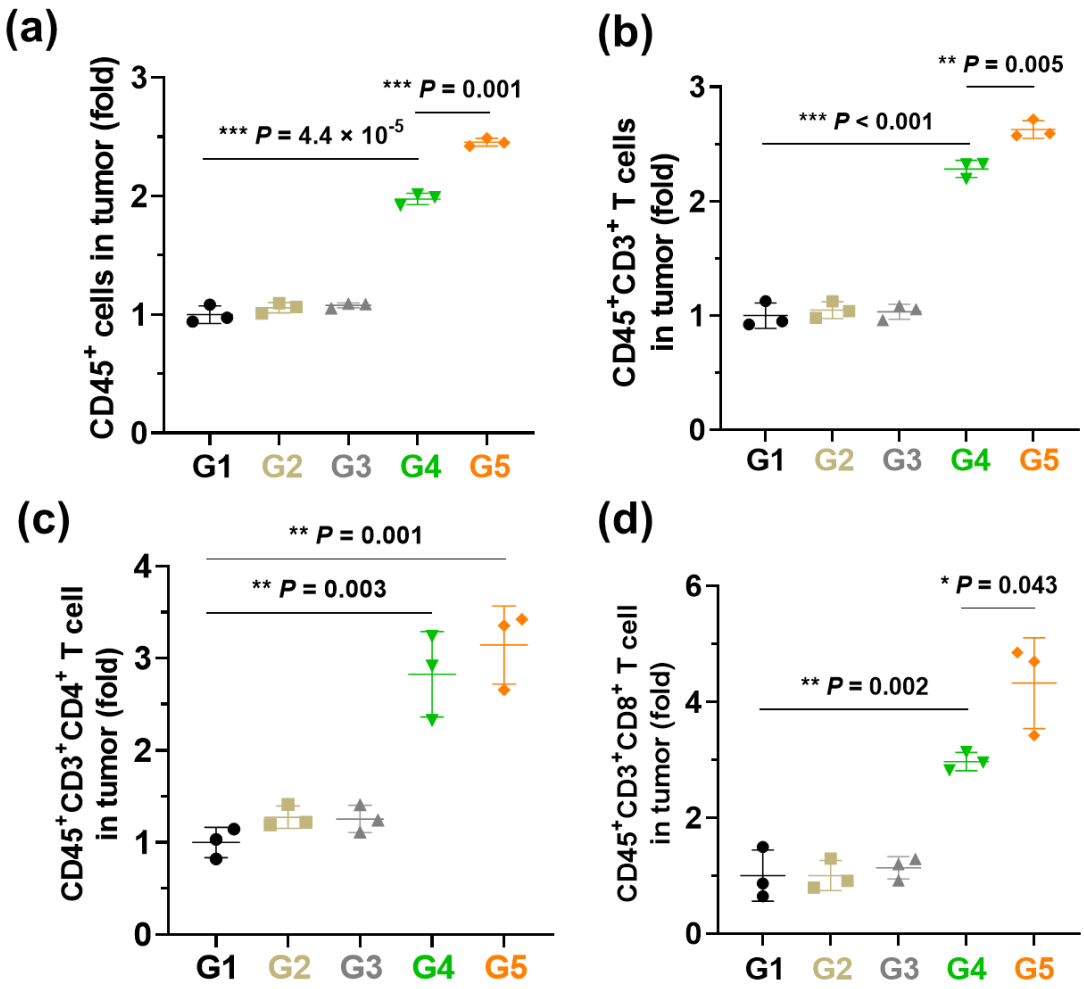

Figure S20. Comparison of immune cell levels in 4T1 tumors in different groups after SnSNPs@PEG-mediated treatment strategy. (a) $CD45^+$ immune cells, (b) $CD45^+CD3^+$ T cells, (c) $CD45^+CD3^+CD4^+$ T cells, and (d) $CD45^+CD3^+CD8^+$ T cells in tumors after various treatments. Data are presented as mean ± SD (n = 3). Statistical analysis between two groups was performed using two-sided student's *t*-test. * $P < 0.05$, ** $P < 0.01$, *** $P < 0.001$. Groups are as follows: control (G1), NIR + US (G2), SnSNPs@PEG (G3), SnSNPs@PEG + US (G4), SnSNPs@PEG + NIR + US (G5), (n = 3).

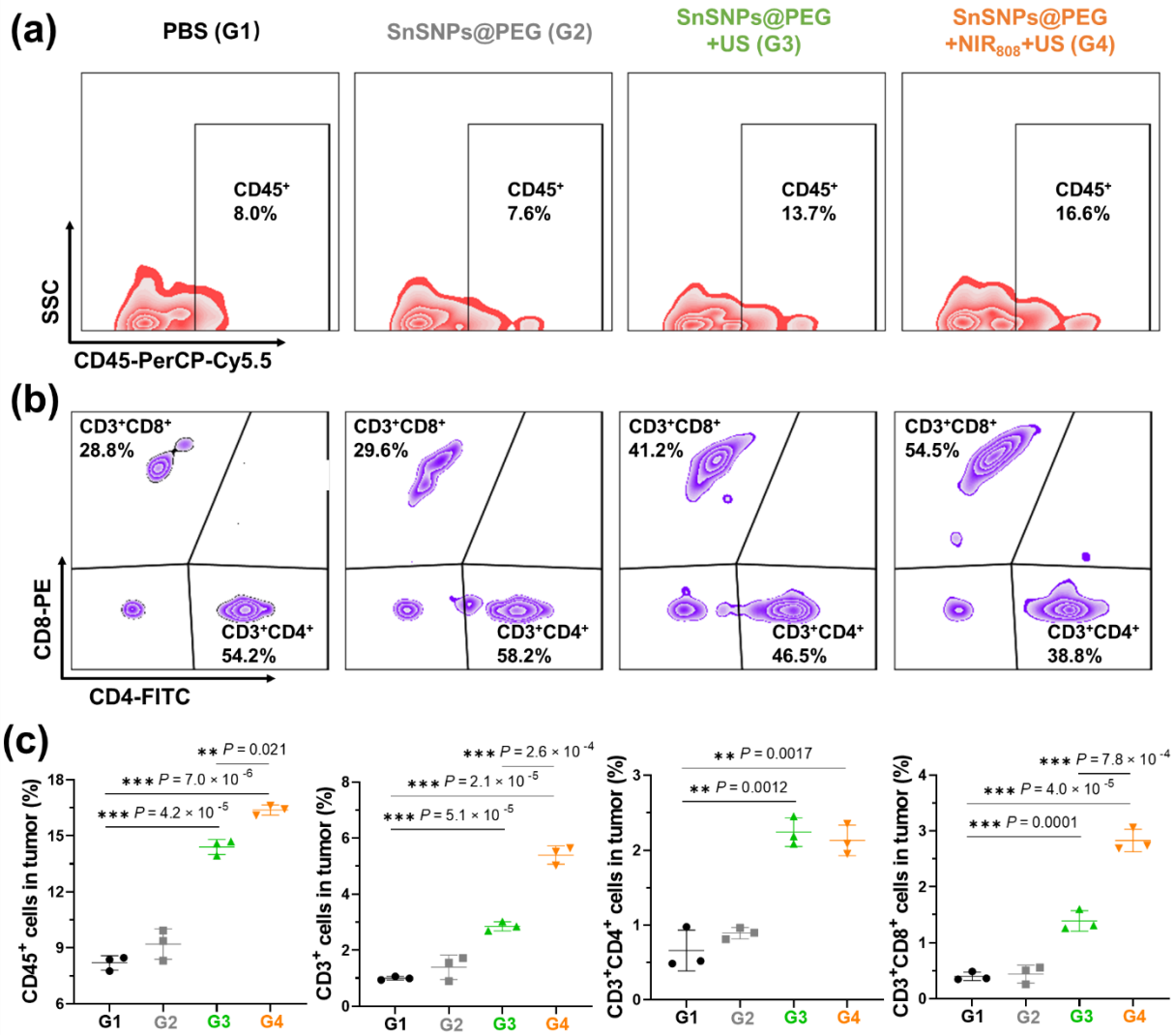

Figure S21. Flow cytometry analysis of (a) $CD45^+$ cells, (b)(c) $CD45^+CD3^+$ lymphocytes, $CD45^+CD3^+CD4^+$ T lymphocytes and $CD45^+CD3^+CD8^+$ T lymphocytes in RIL-175-HCC after different treatments (n = 3). Statistical analysis between two groups was performed using two-sided student's *t*-test. Data are presented as mean ± SD (n = 3) * $P < 0.05$, ** $P < 0.01$, *** $P < 0.001$. Groups are as follows: control (G1), SnSNPs@PEG (G2), SnSNPs@PEG + US (G3), SnSNPs@PEG + NIR + US (G4), (n = 3).

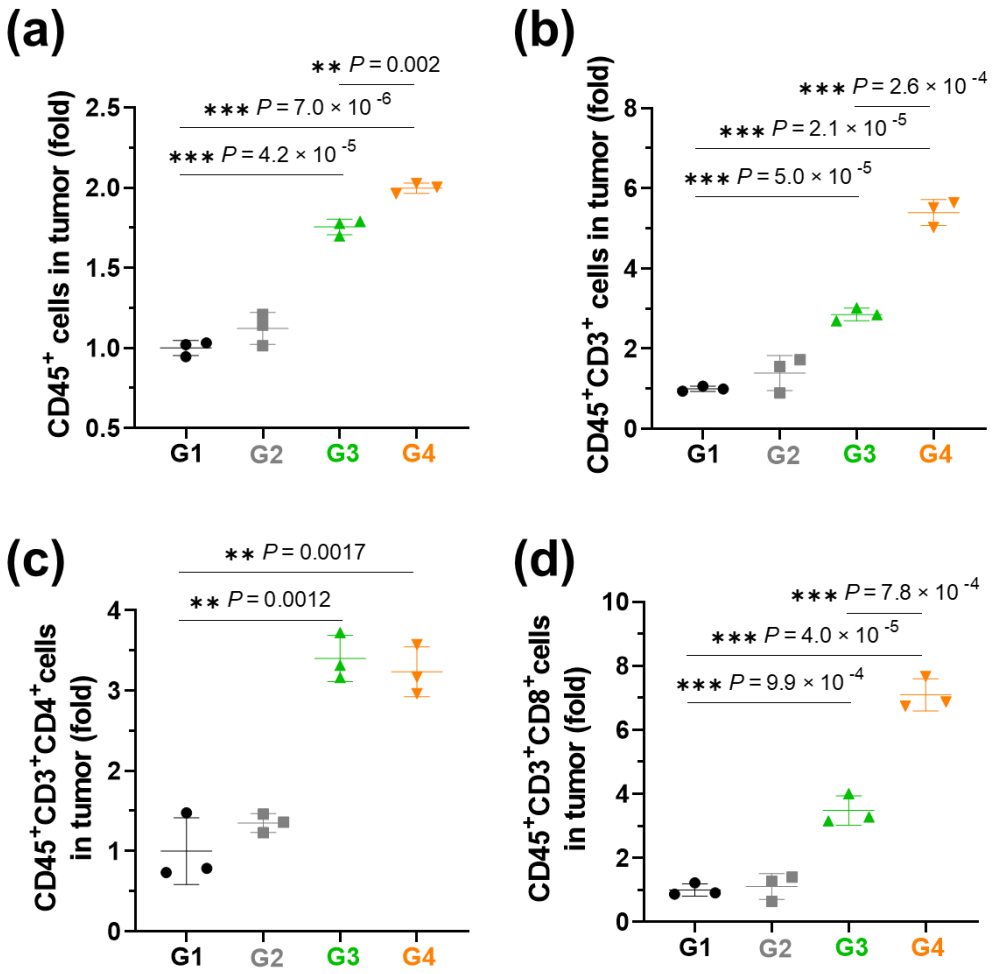

Figure S22. Comparison of the levels of (a) $CD45^+$ immune cells, (b) $CD45^+CD3^+$ T cells, (c) $CD45^+CD3^+CD4^+$ T cells, and (d) $CD45^+CD3^+CD8^+$ T cells in RIL-175-HCC-bearing mice after various treatments (n = 3). Statistical analysis between two groups was performed using two-sided student's *t*-test. Data are presented as mean ± SD (n = 3). * $P < 0.05$, ** $P < 0.01$, *** $P < 0.001$. Groups are as follows: control (G1), SnSNPs@PEG (G2), SnSNPs@PEG + US (G3), SnSNPs@PEG + NIR + US (G4), (n = 3).

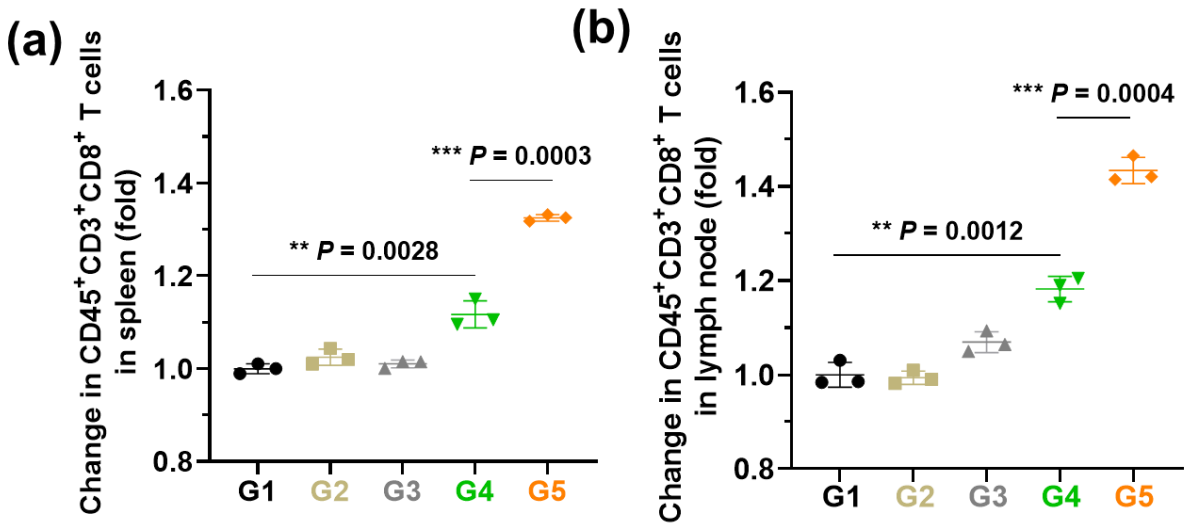

Figure S23. Comparison of $CD45^+CD3^+CD8^+$ T cell levels in spleens and lymph nodes of 4T1 tumor-bearing mice in different groups after SnSNPs@PEG-mediated treatment strategy. (a) spleens and (b) lymph nodes of tumor-bearing mice after various treatments. Statistical analysis between two groups was performed using two-sided student's *t*-test. Data are presented as mean ± SD (n = 3) * $P < 0.05$, ** $P < 0.01$, *** $P < 0.001$. Groups are as follows: control (G1), NIR + US (G2), SnSNPs@PEG (G3), SnSNPs@PEG + US (G4), SnSNPs@PEG + NIR + US (G5), (n = 3).

Table S1. Comparison of the bandgap of SnSNPs with other nano-sonosensitizers.

Sonosensitizer	***Structure***	***Reported bandgap***	***Reference***
SnS	Nanoparticle	1.18 eV	This work
$Bi@BiO_2{-}x@Bi_2S_3$	Nanoparticle	1.43 eV	[1]
α-Fe_2O_3@Pt	Heterostructure particle	1.83 eV	[2]
WOx	Nanobelt	2.11 eV	[3]
$Ti(Oi\text{-}Pr)_4$@Ag	Metal−organic framework	2.11 eV	[4]
Sn	Nanosheet	2.3 eV	[5]
$BiVO_4$	Nanorod	2.5 eV	[6]
Vanadium carbide	Carbon dot	2.57 eV	[7]
Sodium molybdenum bronze	Nanoparticle	2.7 eV	[8]
$TiH_{1.924}$	Nanodot	2.7 eV	[9]
TiO_2	Nanoparticle	3.2 eV	[10]

Table S2. Antibody used for the flow cytometry analysis of T cells.

Antibody	**Brand and Catalog #**	**Concentration for use**
TruStain FcX™ (anti-mouse CD16/32)	Miltenyi Biotec; 130-092-575	1.0 µg/mL
PerCP/Cyanine5.5 anti-mouse CD45	BioLegend; 109828	2.0 µg/mL
APC anti-mouse CD3	BioLegend; 100236	2.5 µg/mL
FITC anti-mouse CD4	BioLegend; 100406	1.5 µg/mL
PE anti-mouse CD8	BioLegend; 100708	1.5 µg/mL

Reference

1. Song, K.*, et al.* Biodegradable Bismuth-Based Nano-Heterojunction for Enhanced Sonodynamic Oncotherapy through Charge Separation Engineering. *Adv. Healthc. Mater.* **11**, e2102503 (2022).
2. Zhang, T.*, et al.* α-Fe_2O_3@Pt heterostructure particles to enable sonodynamic therapy with self-supplied O_2 and imaging-guidance. *J. Nanobiotechnology* **19**, 358 (2021).
3. Zhou, Y.*, et al.* Oxygen-Deficient Tungsten Oxide (WO_x) Nanobelts with pH-Sensitive Degradation for Enhanced Sonodynamic Therapy of Cancer. *ACS Nano* **16**, 17242-17256 (2022).
4. Meng, X.*, et al.* Ag-Doped Metal-Organic Frameworks' Heterostructure for Sonodynamic Therapy of Deep-Seated Cancer and Bacterial Infection. *ACS Nano* **17**, 1174–1186 (2023).
5. Chen, W.*, et al.* Stanene-Based Nanosheets for β-Elemene Delivery and Ultrasound-Mediated Combination Cancer Therapy. *Angew. Chem. Int. Ed.* **60**, 7155-7164 (2021).
6. Yang, Z.*, et al.* Conferring $BiVO_4$ Nanorods with Oxygen Vacancies to Realize Enhanced Sonodynamic Cancer Therapy. *Angew. Chem. Int. Ed.* **61**, e202209484 (2022).
7. Wang, H.*, et al.* A MXene-derived redox homeostasis regulator perturbs the Nrf2 antioxidant program for reinforced sonodynamic therapy. *Chem. Sci.* **13**, 6704-6714 (2022).
8. He, X.*, et al.* NIR-II photo-amplified sonodynamic therapy using sodium molybdenum bronze nanoplatform against subcutaneous Staphylococcus aureus infection. *Adv. Funct. Mater.* **32**, 2203964 (2022).
9. Gong, F.*, et al.* Preparation of $TiH_{1.924}$ nanodots by liquid-phase exfoliation for enhanced sonodynamic cancer therapy. *Nat. Commun.* **11**, 3712 (2020).
10. George, S.*, et al.* Role of Fe doping in tuning the band gap of TiO_2 for the photo-oxidation-induced cytotoxicity paradigm. *J. Am. Chem. Soc.* **133**, 11270-11278 (2011).